Ceramics International 51 (2025) 41948–41958

Contents lists available at ScienceDirect

Ceramics International

journal homepage: www.elsevier.com/locate/ceramint

# Multifunctional europium-doped S53P4 bioactive glass nanocomposites offering magnetic, optical, and antibacterial features for next-generation biomedical applications

Canberk Noyan [a], Emirhan Bakuer [a], Mustafa Burak Coban [b], Mehmet Emin Diken [c], Fatma Unal [a,d,*]

[a] Faculty of Engineering and Natural Sciences, Department of Biomedical Engineering, Samsun University, Samsun, Turkiye
[b] Faculty of Art and Sciences, Department of Physics, Balikesir University, Balikesir, Turkiye
[c] Faculty of Art and Sciences, Department of Molecular Biology and Genetic, Balikesir University, Balikesir, Turkiye
[d] Vocational School of Technical Sciences, Samsun University, Samsun, Turkiye

ARTICLE INFO

Handling Editor: Dr P. Vincenzini

*Keywords:*
Non-invasive bioimaging
Superparamagnetic iron oxide nanoparticles
Magnetic particle imaging
Magneto-luminescent
S53P4 bioactive glass
Nanocomposites

ABSTRACT

The growing demand for multifunctional biomaterials that combine therapeutic and diagnostic functionalities has has led to the development of advanced magneto-luminescent systems. In this study, $Fe_3O_4$ particles coated with $Eu^{3+}$-doped S53P4 bioactive glass were fabricated via a two-step method. High-resolution transmission electron microscopy analysis confirmed a core@shell configuration, with a crystalline $Fe_3O_4$ core and an amorphous $Eu^{3+}$-doped shell. Morphological analyses indicated a transition from spherical to anisotropic structures upon europium incorporation. Magnetic characterization revealed preserved superparamagnetic behavior with a slight decrease in saturation magnetization due to the glass shell. Photoluminescence studies demonstrated strong and tunable photoluminescence without evidence of concentration quenching, as further supported by CIE chromaticity and correlated color temperature (CCT) analyses. Moreover, antibacterial assays indicated significant inhibition of *E. coli* and *S. aureus*, with the optimal activity observed at 1 wt% Eu doping. Owing to their integrated magnetic and optical functionalities, the developed $Fe_3O_4$@$Eu^{3+}$:S53P4 nanocomposites may also serve as potential candidates for magnetic particle imaging (MPI) applications, offering promising perspectives for targeted therapy, real-time tracking, and infection management in orthopedic systems.

## 1. Introduction

The global orthopedic implant market, valued at approximately USD 45.19 billion in 2023, is projected to reach USD 71.74 billion by 2032, highlighting the increasing demand for advanced biomaterials to enhance functional recovery and manage pain in millions of patients worldwide [1]. Despite the benefits provided by orthopedic implants, surgical site infections remain one of the most significant complications, particularly in developing countries. These infections, classified as nosocomial (hospital-acquired) infections, typically occur within one year following surgical procedures involving mechanical or prosthetic material implantation. Their consequences include increased mortality, prolonged hospitalization, and substantial healthcare costs. According to the European Centre for Disease Prevention and Control, infection rates vary between 0.5 % and 9.0 %, depending on the surgical procedure [2]. Specifically, infections occur in approximately 1–3 % of primary implant surgeries, whereas revision surgeries present a reinfection risk as high as 14 %, with an associated mortality rate of 2.5 % [3,4]. Fracture-related osteomyelitis, another severe complication, presents incidence rates ranging from 1.8 % to 28 %, depending on the bone type and fracture severity [5].

The predominant pathogens implicated in orthopedic infections are *Escherichia coli* (*E.coli*) and *Staphylococcus aureus* (*S. aureus*). These microorganisms, by binding to bone through specific extracellular matrix receptors such as fibronectin, laminin, collagen, and sialoglycoproteins, initiate osteomyelitis, which leads to bone destruction and inflammation [2,6–8]. Osteomyelitis, originally described by Edouard Chassaignac in 1852, can involve various anatomical regions of the bone, including the

* Corresponding author. Faculty of Engineering and Natural Sciences, Department of Biomedical Engineering, Samsun University, Samsun, Turkiye.
*E-mail address:* fatma.unal@samsun.edu.tr (F. Unal).

https://doi.org/10.1016/j.ceramint.2025.06.414
Received 23 May 2025; Received in revised form 22 June 2025; Accepted 26 June 2025
Available online 26 June 2025

cortical bone, periosteum, bone marrow, and surrounding soft tissues. This condition may arise not only from traumatic injuries, particularly open fractures, but also as a consequence of internal fixation procedures [6,7,9–11].

A critical factor contributing to the persistence and therapeutic resistance of implant-related infections is bacterial biofilm formation. Biofilms provide a highly protective microenvironment, conferring resistance to antibiotics due to multiple mechanisms: (i) limited antibiotic penetration into the biofilm matrix, (ii) altered metabolic states of bacteria within the biofilm, and (iii) the expression of biofilm-specific phenotypes [12]. Consequently, systemic antibiotic therapies often fail, necessitating localized treatment approaches to overcome the diffusion barriers [9,13–15]. Current local treatment strategies involve the application of antibiotic-loaded polymethyl methacrylate (PMMA) beads, antibacterial bone cements, or bone substitutes [7,16–20]. However, these methods often require invasive surgical interventions for implant removal, extensive debridement of infected tissues, and long-term antibiotic administration [21–24]. In response to these challenges, researchers have explored the development of localized therapeutic systems using biomaterials incorporating antibacterial agents or metallic ions such as silver (Ag), copper (Cu), zinc (Zn), and selenium (Se) [14,25–29]. These innovative materials aim to ddeliver targeted antibacterial activity directly at the infection site, reducing systemic toxicity and promoting tissue regeneration.

Superparamagnetic iron oxide particles ($Fe_3O_4$, SPIONs) have emerged as promising carriers for targeted antibacterial therapies due to their excellent magnetic properties, biocompatibility, and stability [30,31]. SPIONs not only facilitate targeted delivery of therapeutic agents to infection sites but also contribute to bone regeneration by enhancing osteogenic differentiation and cell proliferation, as evidenced by *in vitro* and *in vivo* studies [32–36]. However, accurately monitoring the biodistribution and localization of such carriers remains a significant challenge. To overcome this limitation, SPIONs have been functionally modified with luminescence properties by incorporating lanthanide elements. Lanthanides, renowned for their superior optical characteristics, have been extensively used for biological labeling, enabling non-invasive and real-time imaging of tissues and intracellular structures [30,37–39]. Moreover, lanthanide ions such as europium ($Eu^{3+}$) have demonstrated beneficial effects on bone tissue, promoting osteoblast proliferation and inhibiting osteoclast-mediated bone resorption.

In recent years, there has been a growing emphasis on the development of multifunctional magneto-luminescent materials that simultaneously offer therapeutic efficacy, imaging capability, and real-time monitoring, to address complex biomedical challenges. These materials integrate magnetic and luminescent functionalities within a single platform, enabling targeted therapy, diagnostic imaging, and therapeutic tracking [31,40–48]. For instance, a 2025 study by Das et al. [43] developed sensitizer-passivated magnetic ferrite/$Eu^{3+}$-doped oxide nanocomposites, demonstrating high biocompatibility ($IC_{50} \approx 800$ μg/mL) and strong red luminescence suitable for cellular tracking. The particles effectively induced over 75 % cell death under an alternating magnetic field (AMF) at a dose of just 200 μg/mL, while also showing excellent hemocompatibility (<5 % hemolysis). Similarly, in 2025, Chen et al. [44] introduced $Fe_3O_4/Gd_2O_3:Tb^{3+}@SiO_x$ nanocomposites, tailored for enhanced MRI contrast and demonstrating both *in vitro* cytocompatibility and *in vivo* imaging performance in rat models. Moreover, These results highlight their potential for *in vivo* image-guided magnetic hyperthermia therapy in cancer treatment. In another study, Swain et al. (2024) [45] developed $Fe_3O_4$@$LaF_3$:Eu, Ag@APTES@β-CD nanostructures exhibiting excellent magnetic and luminescent behavior, while also serving as effective carriers for the antibiotic ciprofloxacin, achieving up to 100 % microbial inhibition against *E. coli* and *V. cholerae*. Despite their potential, studies focusing on magneto-luminescent bioactive glasses with antibacterial properties remain scarce [30,42].

Building upon these recent advances, yet addressing the limited integration of bioactivity and antibacterial features in such multifunctional platforms, the present study introduces a novel approach using a bioactive glass matrix. In response to the urgent need for multifunctional biomaterials capable of simultaneously addressing infection control, targeted delivery, and real-time tracking in orthopedic applications, this study proposes the synthesis of superparamagnetic $Fe_3O_4$ particles coated with $Eu^{3+}$-doped S53P4 bioactive glass. By integrating magnetic targeting, tunable photoluminescence for non-invasive optical imaging, and intrinsic antibacterial activity, these engineered nanocomposites aim to serve as an all-in-one theranostic platform. Moreover, the evaluation of their luminescence behavior through CIE chromaticity coordinates and correlated color temperature (CCT) analysis provides novel insights into their optical tunability, establishing a new approach in the development of magneto-luminescent bioactive glasses for advanced biomedical applications. This work aims to lay the groundwork for next-generation multifunctional systems capable of enhancing both the treatment efficacy and monitoring capabilities in orthopedic implant-related infection management and bone tissue engineering. Furthermore, the magnetic properties of the synthesized nanocomposites highlight their potential applicability in magnetic particle imaging (MPI), expanding their prospects for advanced biomedical imaging technologies.

## 2. Materials and methods

### 2.1. Preparation of SPIONs ($Fe_3O_4$)

Multifunctional magneto-luminescent nanocomposites were synthesized using a sequential two-step process. Initially, superparamagnetic iron oxide nanoparticles ($Fe_3O_4$) were synthesized using the co-precipitation method. Iron (III) chloride hexahydrate ($FeCl_3{\cdot}6H_2O$) and iron (II) chloride tetrahydrate ($FeCl_2{\cdot}4H_2O$) were dissolved in 200 mL of deionized water (DI) at a 2:1 M ratio under magnetic stirring at 200 rpm. A 28 % ammonium hydroxide ($NH_4OH$) solution was added dropwise at a rate of approximately 2 drops per second until the pH of the solution reached 9. After the desired pH was achieved, the mixture was further stirred for an additional 15 min at 65 °C to allow complete nanoparticle formation.The resulting solid black particles were subsequently isolated using a neodymium magnet, subjected to thorough washing with deionized water, and finally dried in an oven at $80^0$C.

### 2.2. Preparation of SPIONs coated with bioactive glass

The SPIONs were coated with bioactive glass using a modified Stöber method, aimed at achieving a core/shell particle structure. Initially, 500 mg of dried $Fe_3O_4$ nanoparticles were dispersed in a solution containing 40 mL of ethanol, 10 mL of deionized water, and 3 mL of 28 % ammonium hydroxide. The dispersion was ultrasonicated for 30 min to ensure homogeneous distribution. Separately, tetraethyl orthosilicate (TEOS) was dissolved in 10 mL of ethanol, gradually added to the SPIONs solution, and stirred mechanically for 30 min. Following silica deposition, triethyl phosphate (TEP), calcium nitrate tetrahydrate ($Ca(NO_3)_2{\cdot}4H_2O$), sodium nitrate ($NaNO_3$), and europium nitrate hexahydrate ($Eu(NO_3)_3{\cdot}6H_2O$) were sequentially added in stoichiometric ratios according to the desired S53P4 glass composition (with Eu doping levels ranging from 0.5 to 5 wt%). The reaction mixture was then stirred for 1 h at room temperature to complete the glass precursor hydrolysis-condensation process. The resulting coated nanoparticles were magnetically separated and washed three times via centrifugation (5000 rpm, 5 min) using ethanol and deionized water. The purified nanocomposites were dried in an oven at 80 °C overnight and subsequently subjected to heat treatment in a muffle furnace at 700 °C for 3 h with a heating rate of 5 °C/min to induce glass formation and densification.Detailed sample designations and process parameters are provided in Table 1. The detailed synthesis process was represented in

**Table 1**
Sample designations, and chemical compositions of the core/shell composites. The table represents chemical composition of the bioactive glass shell. The $Fe_3O_4$ core is not included in this composition.

| Sample Designation | Chemical Composition (wt%) | | | | |
|---|---|---|---|---|---|
| | $P_2O_5$ | CaO | $Na_2O$ | $SiO_2$ | $Eu_2O_3$ |
| $Fe_3O_4$@S53P4 | 4 | 20 | 23 | 53 | 0 |
| $Fe_3O_4$@0.5Eu:S53P4 | 4 | 20 | 23 | 52.5 | 0.5 |
| $Fe_3O_4$@1.5Eu:S53P4 | 4 | 20 | 23 | 51.5 | 1.5 |
| $Fe_3O_4$@3Eu:S53P4 | 4 | 20 | 23 | 50 | 3 |
| $Fe_3O_4$@5Eu:S53P4 | 4 | 20 | 23 | 48 | 5 |

Fig. 1.

### 2.3. Materials characterization

The structural, morphological, magnetic, and optical properties of the synthesized particles were characterized using various techniques. X-ray diffraction (XRD) was performed using a Philips PW3710 X'Pert Pro diffractometer equipped with monochromatic $CuK_\alpha$ radiation, operating over a 2θ range of $20^0$ - $80^0$ at a scanning rate of $2^0$/min, to identify the crystalline phases. Fourier-transform infrared spectroscopy (FT-IR) measurements were carried out using a PerkinElmer Spectrum Two spectrometer to investigate the functional groups and chemical composition of the particles. Surface morphology was examined via scanning electron microscopy (SEM) at magnifications of 50,000x, 100,000x, and 200,000x, using an acceleration voltage of 20 kV and a working distance (WD) of 9.8 mm. Detailed structural features were elucidated using transmission electron microscopy (TEM) and high-resolution TEM (HR-TEM) with a FEI TALOS F200S instrument at an acceleration voltage of 200 kV. Magnetic characterization were performed using a Vibrating Sample Magnetometer (VSM, Model 7407, Lakeshore) under magnetic fields ranging from −10,000 Oe to +10,000 Oe. Furthermore, photoluminescence (PL) measurements were conducted using a 349 nm excitation source with the ANDOR SR500i spectrometer to evaluate the optical behavior of undoped and europium-doped nanocomposites.

### 2.4. Antibacterial investigations

The antibacterial activity of the synthesized nanoparticles was systematically assessed against *E. coli* and *S. aureus* using the agar well diffusion method. Bacterial cultures were grown in Nutrient Broth to a concentration of approximately $2.4 \times 10^5$ CFU/mL. Subsequently, 6 mm diameter wells were prepared on Nutrient Agar plates, into which 10 mg of each sample was carefully placed. The plates were then incubated at 37 °C for 18–24 h under aerobic conditions. Following incubation, the diameter of the inhibition zones surrounding each well was measured using a standard scale to assess antibacterial efficacy. All experiments were conducted in triplicate to ensure reproducibility. The formation of a clear inhibition zone around the well indicated effective antibacterial activity of the tested samples.

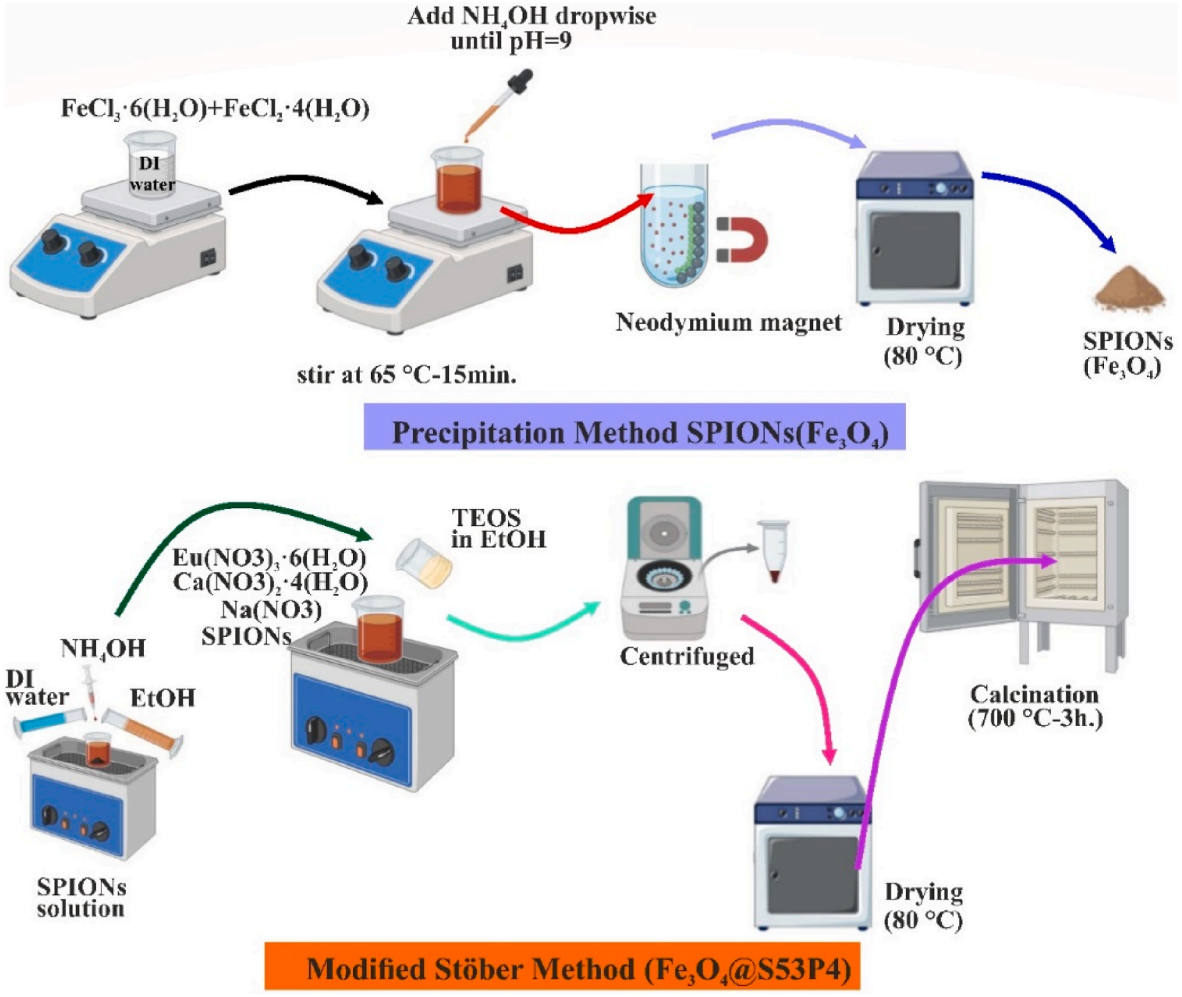


**Fig. 1.** Schematic illustration of the fabrication process.

## 3. Results and discussions

### 3.1. XRD and FT-IR analysis

Fig. 2a presents the X-ray diffraction (XRD) patterns of the $Fe_3O_4$@S53P4 and $Fe_3O_4$@5Eu:S53P4 nanocomposites. The diffraction peaks observed in both samples were indexed to the standard cubic magnetite structure of $Fe_3O_4$ (*Fd-3m space group*), consistent with JCPDS card no. 075–0449 [30,31]. Characteristic reflections appeared at 2θ values of $30.52^0$, $35.58^0$, $43.20^0$, $53.72^0$, $63.07^0$, and $74.75^0$, corresponding to the (220), (311), (400), (422), (511), and (440) crystallographic planes, respectively. Importantly, no additional peaks corresponding to the S53P4 bioglass phase were observed, confirming the amorphous nature of the bioglass matrix. Furthermore, no significant shifts or changes in the peak positions were observed upon $Eu^{3+}$ doping, suggesting that the dopant incorporation did not alter the crystalline structure of the $Fe_3O_4$ core.

Fig. 2b shows the FTIR spectra of $Fe_3O_4$@S53P4, $Fe_3O_4$@1.5Eu:S53P4 and $Fe_3O_4$@5Eu:S53P4 samples. The observed vibrational bands and their corresponding assignments for the bioglass structures are also provided in the figure. It can be observed that, the undoped nanoaprticles ($Fe_3O_4$@S53P4) shows the characteristic absorption bands at approximately 452 $cm^{-1}$, 797 $cm^{-1}$ and 1063 $cm^{-1}$ which are attributed to the Si-O-Si bending mode, Si-O-Ca stretching mode and P-O bending mode, respectively. Additionally, the weak vibrational modes observed at 549 and 642 $cm^{-1}$ are characteristic vibrations of Fe-O for SPIONs, and the presence of the peak at 549 $cm^{-1}$ was attributed to the Fe-O strain mode of magnetite (core, $Fe_3O_4$) [30,49,50]. Upon $Eu^{3+}$ doping, slight variations in the intensity and position of the vibrational peaks are observed. Among the samples shown, the band intensities associated with the Si–O–Si and P–O groups appear stronger in the $Fe_3O_4$@1.5Eu:S53P4 sample compared to the undoped and $Fe_3O_4$@5Eu:S53P4 samples. Furthermore, the absorption band around 803 $cm^{-1}$, corresponding to the symmetric stretching mode of Si–O–Ca, is not visible in the FTIR spectrum of the $Fe_3O_4$@5Eu:S53P4 sample. A broad band near 1493 $cm^{-1}$ is also observed only in the 5 wt% Eu-doped sample, which is attributed to the stretching vibration of –OH groups and atmospheric moisture absorption.

### 3.2. SEM analysis

Fig. 3 presents SEM micrographs of the synthesized samples at magnifications of 50,000x, 100,000x, and 200,000x. Images (a), (b), and (c) correspond to $Fe_3O_4$@S53P4, while (d), (e), and (f) show $Fe_3O_4$@5Eu:S53P4 particles. The $Fe_3O_4$@S53P4 sample exhibits a predominantly spherical and compact morphology, with noticeable particle agglomeration. This appearance is typical for powder materials synthesized via wet chemical methods and suggests relatively uniform nucleation during synthesis. In contrast, the $Fe_3O_4$@5Eu:S53P4 nanocomposites display a distinctly anisotropic morphology, with plate-like, or leaf-like structures. The incorporation of $Eu^{3+}$ ions appears to influence the particle growth mechanism, leading to a variation in structural organization. Overall, SEM analysis indicates that $Eu^{3+}$ doping alters the morphology of the particles compared to the undoped sample.

### 3.3. TEM analysis

As shown in Fig. 4a–c, the TEM and HR-TEM images of the undoped $Fe_3O_4$@S53P4 bioactive glass nanocomposites reveal a well-defined core@shell structure. ImageJ software analysis indicated that the average particle size of the $Fe_3O_4$ cores was approximately 15.0 ± 3.0 nm, based on measurements from 120 individual particles. The corresponding particle size distribution histogram (Fig. 4b) confirms the relatively narrow size distribution, supporting the morphological uniformity of the synthesized nanoparticles. HR-TEM imaging (Fig. 4c) clearly shows a crystalline $Fe_3O_4$ core encapsulated by an amorphous S53P4 bioactive glass shell. Furthermore, the measured interplanar spacing (*d*-spacing) for the (220) plane was approximately 2.92 Å, which is in close agreement with the standard value reported for the cubic magnetite structure of $Fe_3O_4$. These observations further corroborate the XRD results, reinforcing the distinct structural features of the core and shell regions.

### 3.4. Magnetic properties

The magnetization curves are presented in Fig. 5. Both $Fe_3O_4$@S53P4 and $Fe_3O_4$@5Eu:S53P4 bioactive glass nanocomposites exhibited superparamagnetic behavior at room temperature, as indicated by the absence of coercivity and remanent magnetization in the magnetic hysteresis loop. The saturation magnetization ($\sigma_s$) values were determined to be 13.81 emu/g for $Fe_3O_4$@S53P4 and 12.01 emu/g for $Fe_3O_4$@5Eu:S53P4 particles. The incorporation of $Eu^{3+}$ ions into the bioactive glass matrix may have caused a slight decrease in the saturation magnetization due to the non-magnetic nature of the glass shell and the dilution of the magnetic moment. Notably, these values are higher than those reported for similar multifunctional core-shell nanostructures such as $Fe_3O_4$@$SiO_2$@$Y_2O_3$:$Eu^{3+}$ systems, which exhibit saturation magnetizations in the range of 9.34–11.6 emu/g at room temperature

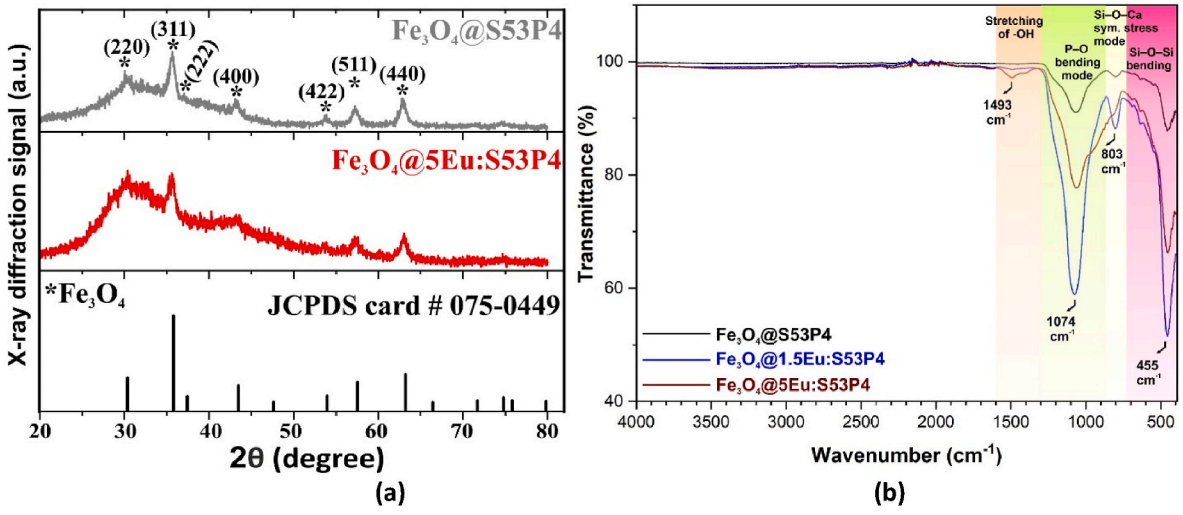


**Fig. 2.** **(a)** XRD patterns of $Fe_3O_4$@S53P4, and $Fe_3O_4$@5Eu:S53P4 and **(b)** FT-IR spectra of $Fe_3O_4$@S53P4, $Fe_3O_4$@1.5Eu:S53P4and $Fe_3O_4$@5Eu:S53P4.

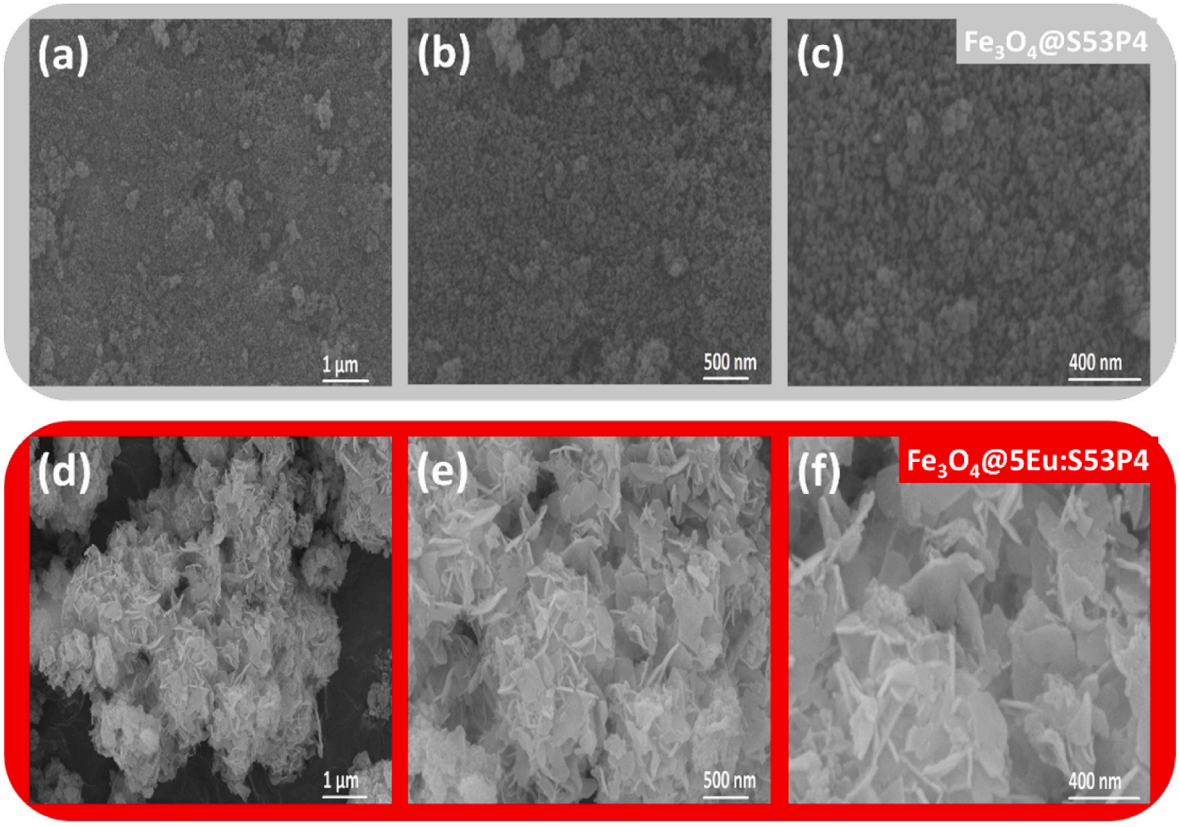


**Fig. 3.** SEM micrographs of nanocomposites captured at 50,000x, 100,000x and 200,000x magnifications (a, b, c) $Fe_3O_4$@S53P4, and (d, e, f) $Fe_3O_4$@5Eu:S53P4.

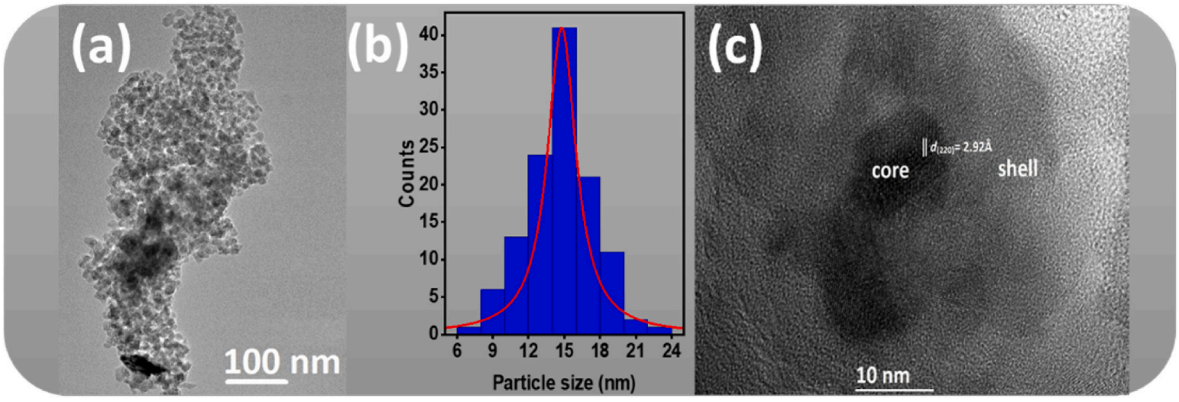


**Fig. 4.** (a) TEM, (b) particle size distribution graph of and (c) HR-TEM images of $Fe_3O_4$@S53P4.

depending on $Eu^{3+}$ concentration [40]. Additionally, silica-coated $Fe_3O_4$ particles with varying shell thicknesses have been demonstrated even lower $\sigma_s$ values (5.38–9.29 emu/g) due to magnetic mass dilution [41]. These comparisons highlight that our nanocomposites retain strong magnetic responsiveness while simultaneously offering luminescent and antibacterial functionalities, positioning them as promising candidates for advanced theranostic applications.

### 3.5. PL properties

Photoluminescence (PL) spectroscopy is a valuable method for investigating the behavior of energy and charge carriers in materials upon light excitation. In this process, atoms or molecules absorb external electromagnetic radiation, become excited, and subsequently return to their ground state by emitting photons. By analyzing the emitted light, researchers can obtain valuable information about the electronic structure, defects, and energy transfer mechanisms of the material. PL spectroscopy is widely used in various fields, including materials science, physics and chemistry, as it provides valuable information about the energy transfer mechanisms and electronic properties of different substances. It offers a non-destructive and highly sensitive approach to studying the interactions between light and matter, enabling the scientific community to better understand the fundamental processes involved in photoluminescence and how they can be utilized in various applications [51]. In the context of this study, it is extremely important to determine the responses of doped and undoped S53P4 bioactive glasses according to the current excitation source and to compare them with each other, especially in terms of paving the way for biomedical research, which has accelerated in recent years. As seen in Fig. 6, $Eu^{3+}$ ions were incorporated into bioactive glasses at concentrations ranging

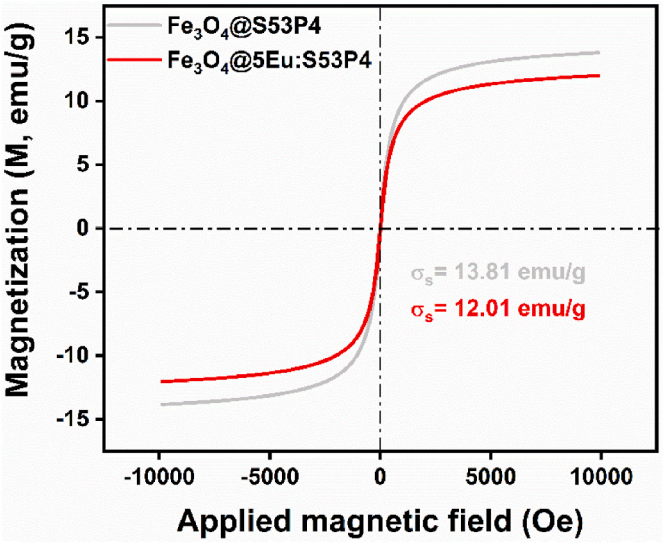


**Fig. 5.** Magnetic hysteresis curves of $Fe_3O_4$@5S53P4, and $Fe_3O_4$@5Eu:S53P4.

from 0.5 to 5 wt%, in order to gain a better understanding of their luminescence behavior and optimize their performance for potential biomedical imaging and therapeutic applications.

Fig. 6 shows the effect of doped bioactive glass on the luminescence profile and thus on its structural properties. $Eu^{3+}$ ions were used as spectroscopic probes. Under the 349 nm laser excitations, the emission spectra indicate five emissions at 577, 593, 612, 653, and 703 nm which are related to the $^5D_0 \rightarrow {}^7F_{0,1,\,2,\,3,\,4}$ transitions, respectively (Fig. 6a and e). The intense electric dipole transitions $^5D_0 \rightarrow {}^7F_{2,4}$ at 612 and 703 nm depend entirely on the environment of the host matrix in which the luminescence centers are embedded. $^5D_0 \rightarrow {}^7F_1$ at 593 nm is a magnetic dipole transition, which is almost unaltered by the crystal field strength around $Eu^{3+}$, allowed by Laporte's selection rule and is independent of the glass medium. In the present matrix, the emission intensity of the electric dipole transition is higher than that of the magnetic dipole transition, indicating that $Eu^{3+}$ ions are surrounded by a non-centrosymmetric crystal field region [52].

The local inversion symmetry around europium ions is determined by the ratio of the electric dipole transition ($^5D_0 \rightarrow {}^7F_2$) to the magnetic dipole transition ($^5D_0 \rightarrow {}^7F_1$) as follows [53–55]:

$$R \Big/ O = \left({}^5D_0 \rightarrow {}^7F_1 \Big/ {}^5D_0 \rightarrow {}^7F_1\right) = \frac{I_{612}}{I_{593}}$$

The asymmetry ratio of the samples was determined to increase from 1.12 (0.005 doping ratio) to 1.79 (0.05 doping ratio). Lower R/O ratios typically indicate higher crystal field symmetry. The calculated asymmetry ratio is found to grow slightly and reaches a maximum at a concentration of 0.05. This asymmetry ratio is approximately equal to 2, indicating that $Eu^{3+}$ also occupies non-centrosymmetric sites [56].

At low $Eu^{3+}$ doping levels, the incorporation of $Eu^{3+}$ activator ions into the lattice leads to a gradual increase in PL intensity, primarily due to enhanced absorption of excitation photons. However, as the $Eu^{3+}$ concentration exceeds a critical threshold, the distance between luminescent activator ions decreases, thereby increasing the probability of non-radiative energy transfer. This occurs as a natural consequence of the increased probability of cross-relaxation transitions between the emitting ions, leading to a decrease in the radiative emission efficiency. In the present study, the distance between the $Eu^{3+}$ ions is still not sufficiently reduced and non-radiative processes cannot be observed.

Deliormanlı et al. synthesized $Dy^{3+}$ and $Eu^{3+}$ doped 5-fluorouracil bioactive glasses by sol-gel technique. To analyze the luminescence potential of the bioactive glasses, emission spectra were obtained by excitation at 305, 337 and 375 nm. These excitation wavelengths closely match the excitation source employed in our study, thereby enabling meaningful comparisons of luminescence efficiency. The luminescence results show that no concentration quenching was observed, similar to what we now report [52]. Xue et al. fabricated $Eu^{3+}$-doped bioactive glass nanoparticles by sol-gel synthesis and presented their controllable drug delivery, cell imaging and luminescence properties in detail. The current results demonstrate that the luminescence intensity increases with $Eu^{3+}$ concentration without exhibiting concentration quenching, with the highest emission intensity observed in the BGN-$Eu^{3+}$ bioactive glass nanoparticles [57]. Another focal point of this study is that when the luminescence spectrum is analysed, $Eu^{3+}$ characteristic peaks as well as a broadband spectrum are observed, indicating that the host bioactive glass nanospheres cannot transfer energy transfer at a sufficient level and contribute to luminescence. In our present report, no broadband emission from the bioactive glasses was observed and an effective energy transfer according to the improved luminescence phenomenon was attributed to the transfer of $Eu^{3+}$ ions, which act as luminescence activators, from the bioactive glass spheres.

Fig. 6c also shows how the dopant concentration affects the PL peak intensities of 5S3P4:Eu3+. As seen in the data in the figure, the highest PL intensity occurs at a dopant concentration of 0.5 wt%. As the dopant concentration increases from 0.005 to 0.05, the PL emission intensity first increases slightly with increasing dopant concentration, followed by a very slight increase from 0.015 to 0.03. However, when the dopant concentration increases from 0.03 to 0.05, a drastic increase is clearly observed. However, the concentration quenching phenomenon was not observed. The reason for this phenomenon is that the $Eu^{3+}$ additive concentration is not sufficient to cause defects that produce additional PL, and as a result, the integrated PL intensity did not exhibit concentration quenching.

Fig. 6d represents the CIE 1931 chromaticity diagram used to analyze the colorimetric properties of $Fe_3O_4$@Eu:S53P4 bioactive glass nanoparticles. The emission colour was observed to change from the blue-green region to the white region with increasing $Eu^{3+}$ concentration, indicating a tunable luminescence. The CIE chromaticity coordinates (x, y) for each $Eu^{3+}$ doping level are included as insets in Fig. 6c and provide a detailed illustration of this colour variation. To further evaluate the emission properties, the correlated colour temperature (CCT) was calculated using the following McCamy empirical equation [58]:

$$T_c = -449n^3 + 3525n^2 - 6823.3n + 5520.33$$

where $T_c$ represents the color temperature (in Kelvin), and $n$ is defined as:

$$n = \frac{(x - 0.3320)}{(y - 0.1858)}$$

where (x,y) are the CIE colour coordinates. For cool white light applications, CCT values above 5000 K are known to be suitable. For increasing $Eu^{3+}$ concentrations, the calculated CCT values show a gradual decrease from 6826 K to 5504 K. For a doping concentration of 0.05, the CCT value is 5504 K, indicating that the transition from cool white to neutral white is approaching, making them suitable candidates for solid state lighting and display applications [59].

The evaluation of the colour purity for the emitting colour is important to study the effect of $Eu^{3+}$ incorporation in narrow-band light sources. The colour purity of phosphors was calculated using equation [60–62]:

$$\text{Color Purity} = \sqrt{\frac{(x - x_i)^2 + (y - y_i)^2}{(x_d - x_i)^2 + (y_d - y_i)^2}} \times 100$$

where (x, y) are the color coordinates of the sample, (xi, yi) are the chromaticity coordinates of the white illuminant (0.333, 0.333) and (xd, yd) are the coordinates of the dominant wavelength in the emission.

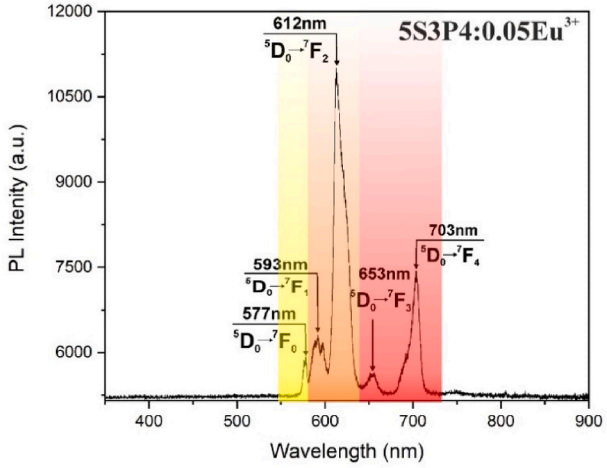
612nm
$^5D_0 \rightarrow ^7F_2$
5S3P4:0.05Eu$^{3+}$
593nm
$^5D_0 \rightarrow ^7F_1$
577nm
$^5D_0 \rightarrow ^7F_0$
653nm
$^5D_0 \rightarrow ^7F_3$
703nm
$^5D_0 \rightarrow ^7F_4$
PL Intenity (a.u.)
Wavelength (nm)

(a)

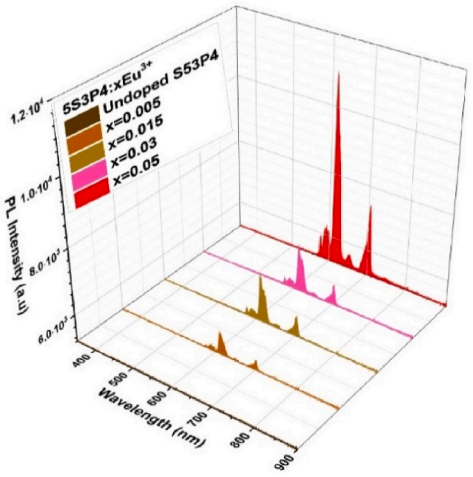
5S3P4:xEu$^{3+}$
Undoped S53P4
x=0.005
x=0.015
x=0.03
x=0.05
PL Intensity (a.u)
Wavelength (nm)

(b)

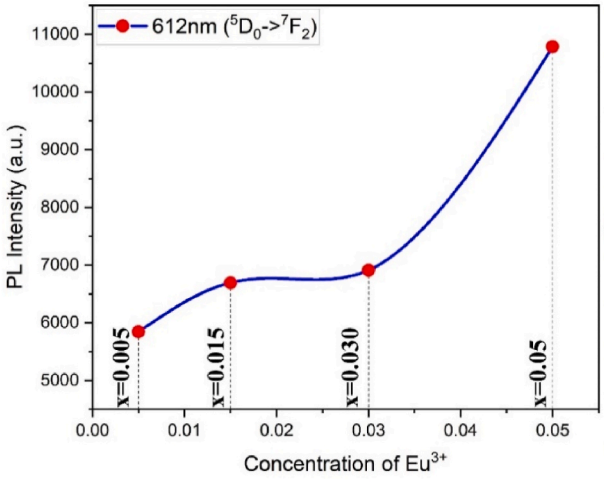
612nm ($^5D_0$->$^7F_2$)
PL Intensity (a.u.)
x=0.005
x=0.015
x=0.030
x=0.05
Concentration of Eu$^{3+}$

(c)

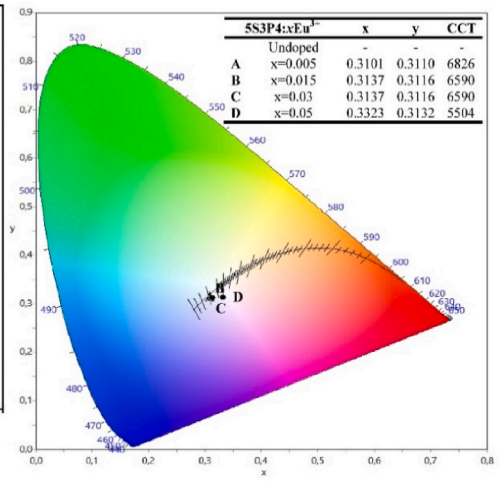
5S3P4:xEu$^{3+}$ | x | y | CCT
Undoped | - | - | -
A | x=0.005 | 0.3101 | 0.3110 | 6826
B | x=0.015 | 0.3137 | 0.3116 | 6590
C | x=0.03 | 0.3137 | 0.3116 | 6590
D | x=0.05 | 0.3323 | 0.3132 | 5504

(d)

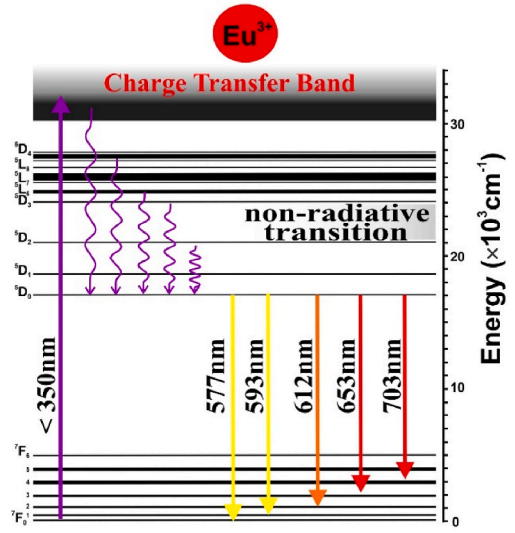
Eu$^{3+}$
Charge Transfer Band
non-radiative transition
< 350nm
577nm
593nm
612nm
653nm
703nm
Energy (×10$^3$cm$^{-1}$)

(e)

**Fig. 6.** (a) PL emission spectrum of $Fe_3O_4$@0.5Eu:S53P4, (b) 3D PL intensity map of all the particles, (c) The dependence of $Eu^{3+}$ emission intensity at 612 nm ($^5D_0 \rightarrow {}^7F_2$) as a function of the $Eu^{3+}$ content (d) CIE chromaticity diagram, (e) Schematic energy level diagram of $Eu^{3+}$ illustrating charge transfer and radiative transitions.

Here, the wavelength corresponding to the $^5D_0$ - $^7F_2$ transition is taken as the dominant wavelength and hence (xd, yd) = (0.67, 0.33) in this work. The $Eu^{3+}$ concentration ranges from x = 0.5 to x = 5 and the color purity ranges from 5.84 % to 9.37 % (Table 2). When all these results are combined with the trend towards the white region in the CIE chromaticity coordinates and the CCT color correlation temperature, the material we have developed will be a suitable candidate for solid-state lighting and WLED's applications [51].

### 3.6. Antibacterial activity

Table 3 and Fig. 7 illustrate the antibacterial performance of the synthesized nanocomposites against *Staphylococcus aureus* (*S. aureus*, Gram-positive) and *Escherichia coli* (*E. coli*, Gram-negative), which are widely employed as representative indicator strains in antibacterial efficacy assessments. It was observed that all nanocomposites showed activity against both bacterial species. Notably, variations in antibacterial activity were observed with the incorporation of $Eu^{3+}$ into the nanocomposites. Europium, a rare earth element, is known to possess concentration-dependent antimicrobial properties, and its presence significantly enhanced the ability of the nanocomposites to inhibit bacterial growth and potentially prevent biofilm formation [61,63]. The effectiveness of Eu in inhibiting bacterial growth and biofilm formation is influenced by its concentration, which affects its interaction with bacterial cells and the generation of reactive species that can damage bacterial structures [64]. Also, another aspect of the nanocomposites indicates that the capacity of $Fe_3O_4$ magnetic nanoparticles to induce microbial toxicity stems from various interactions; encompass membrane depolarization leading to the compromise of cellular integrity, lipid peroxidation, and DNA damage, in addition to the generation of reactive oxygen species and the liberation of metal ions that disrupt cellular homeostasis and protein coordination [65]. In this study, the antibacterial effect of them prepared by adding Eu (0.5 wt%.) at the lowest concentration was the highest than other samples. It is observed that the activity decreased significantly with increasing amount of Eu element. The synthesized samples were found to be more effective against gram-positive *S. aureus*.

Overall, $Fe_3O_4$@Eu:S53P4 core@shell structured bioactive glass particles were successfully synthesized to integrate magnetic, luminescent, and antibacterial functionalities into a single platform. The XRD results confirmed the preservation of the crystalline magnetite cubic structure of the $Fe_3O_4$ core, while the S53P4 bioactive glass shell remained amorphous, even after europium doping. The structural integrity of the particles was further supported by TEM and HR-TEM analyses, revealing a clear distinction between the crystalline core and the amorphous shell with an average particle size of approximately 15 nm.

SEM imaging indicated a morphological shift upon europium incorporation, transitioning from spherical forms to more anisotropic, leaf-like structures. This morphological evolution suggests that the addition of Eu element influenced the nucleation and growth processes during synthesis, consistent with previously reported effects of lanthanide doping on sol-gel derived systems.

**Table 2**
The CIE coordinates, CCT values Colour Purity range of Eu-doped nanocomposites.

| | CIE Chromaticty Coordinates (x,y) | | CCT value (K) | CP (%) |
|---|---|---|---|---|
| $Fe_3O_4$@0.5Eu:S53P4 | 0.3101 | 0.3110 | 6826 | 9.37 |
| $Fe_3O_4$@1.5Eu:S53P4 | 0.3137 | 0.3116 | 6590 | 8.50 |
| $Fe_3O_4$@3Eu:S53P4 | 0.3137 | 0.3116 | 6590 | 8.50 |
| $Fe_3O_4$@5Eu:S53P4 | 0.3323 | 0.3132 | 5504 | 5.84 |

**Table 3**
Antibacterial activities of all the particles against *E. coli* and *S. aureus*.

| Sample | Inhibition zone (mm) | |
|---|---|---|
| | E. coli | S. aureus |
| $Fe_3O_4$@S53P4 | 7.48 ± 0.09 | 8.61 ± 1.76 |
| $Fe_3O_4$@0.5Eu:S53P4 | 8.35 ± 0.12* | 11.50 ± 0.20* |
| $Fe_3O_4$@1.5Eu:S53P4 | 7.34 ± 0.53 | 9.09 ± 0.56* |
| $Fe_3O_4$@3Eu:S53P4 | 6.96 ± 0.39 | 8.45 ± 0.42 |
| $Fe_3O_4$@5Eu:S53P4 | 6.94 ± 0.42 | 8.61 ± 0.078 |
| Penicillin/Streptomycin | 24.95 ± 2.55** | 23.40 ± 1.60** |

*p<0.05 – statically significant, **p<0.001 – highly statically significant.

Magnetic characterization demonstrated that both undoped and Eu-doped particles retained superparamagnetic behavior, which is crucial for targeted delivery applications. A slight decrease in saturation magnetization upon Eu doping was attributed to the non-magnetic nature of the glass shell and potential magnetic dilution effects, aligning with findings reported in similar multifunctional nanocomposite studies.

Photoluminescence analyses revealed characteristic $Eu^{3+}$ emissions without evidence of concentration quenching, even at the highest doping level investigated. The tunable luminescence, as verified by CIE chromaticity analysis and correlated color temperature (CCT) calculations, indicated a promising potential for optical tracking and imaging applications.

Furthermore, antibacterial assessments confirmed the efficacy of the synthesized particles against both *E. coli* and *S. aureus*, with the highest inhibition observed at the lowest Eu doping level. The observed antibacterial properties are thought to arise from the synergistic effects of the $Fe_3O_4$ core and the $Eu^{3+}$ ions incorporated into the bioactive glass matrix.

Taken together, the results demonstrate that Eu-doped particles hold significant promise for multifunctional biomedical applications that require the integration of magnetic responsiveness, optical traceability, and antibacterial performance. In particular, these materials show strong potential for addressing challenges associated with orthopedic implant-related infections, bone tissue engineering, and non-invasive bioimaging applications, where simultaneous therapeutic and diagnostic capabilities are highly desirable.

## 4. Conclusions

In this study, multifunctional $Fe_3O_4$@Eu:S53P4 bioactive glass particles were successfully synthesized through a two-step method involving co-precipitation and a modified Stöber process. The structural characterization confirmed the formation of core@shell architecture, featuring a crystalline $Fe_3O_4$ core and an amorphous $Eu^{3+}$-doped S53P4 bioactive glass shell.

Morphological observations revealed that $Eu^{3+}$ doping influenced the particle growth behavior, resulting in a transition from spherical to more anisotropic, leaf-like structures. Furthermore, HR-TEM analyses confirmed the formation of a core@shell architecture, where the crystalline $Fe_3O_4$ core was surrounded by an amorphous S53P4 bioactive glass shell. The average particle size was determined to be approximately 15 nm. HR-TEM imaging also revealed an interplanar spacing of 2.92 Å corresponding to the (220) plane of the cubic magnetite $Fe_3O_4$ structure, further corroborating the findings obtained from XRD.

Magnetic measurements demonstrated that both doped and undoped

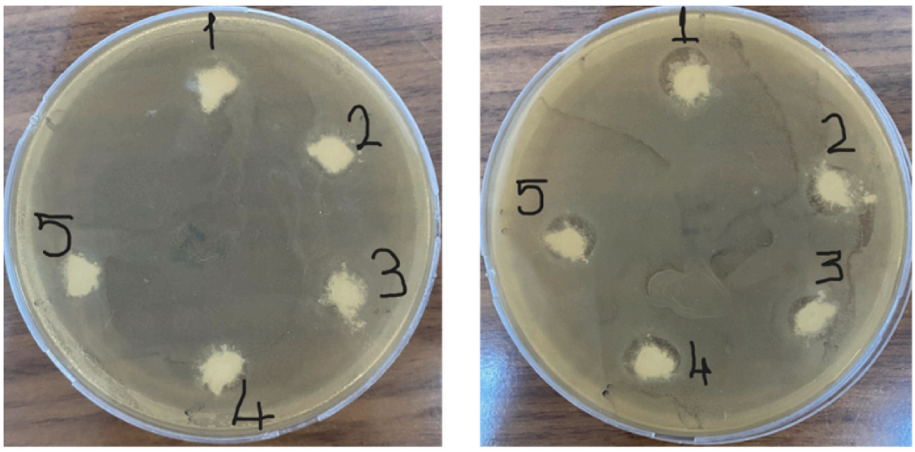


**Fig. 7.** Inhibition zone of all components against to *E. coli* (a) and *S. aureus* (b): (1-$Fe_3O_4$@S53P4, 2-$Fe_3O_4$@0.5Eu:S53P4, 3-$Fe_3O_4$@1.5Eu:$S5_3P_4$, 4-$Fe_3O_4$@3Eu:S53P4, 5-$Fe_3O_4$@5Eu:S53P4).

particles exhibited superparamagnetic behavior, which is critical for magnetic targeting applications. A slight decrease in saturation magnetization was observed upon $Eu^{3+}$ doping, attributed to the non-magnetic nature of the glass shell.

Photoluminescence characterization showed strong and tunable $Eu^{3+}$ emissions without concentration quenching, as validated by CIE chromaticity analysis and correlated color temperature (CCT) evaluations. These results highlight the potential of the particles for optical tracking and non-invasive bioimaging. Additionally, antibacterial investigations showed that all synthesized particles exhibited activity against both *E. coli* and *S. aureus*, with the highest antibacterial performance observed at lower $Eu^{3+}$ doping levels.

Taken together, these findings demonstrate that $Fe_3O_4$@Eu:S53P4 particles represent a promising multifunctional platform that integrates magnetic responsiveness, optical traceability, and antibacterial activity. With their combined therapeutic and diagnostic capabilities, these particles are strong candidates for applications in orthopedic implant-related infection management, bone tissue engineering, and advanced theranostic strategies, including non-invasive bioimaging and magnetic particle imaging (MPI).

## CRediT authorship contribution statement

**Canberk Noyan:** Methodology. **Emirhan Bakuer:** Methodology. **Mustafa Burak Coban:** Writing – original draft, Validation, Resources, Methodology, Investigation. **Mehmet Emin Diken:** Writing – original draft, Validation, Resources, Methodology. **Fatma Unal:** Writing – original draft, Validation, Supervision, Resources, Project administration, Methodology, Investigation, Funding acquisition, Conceptualization.

## Declaration of competing interest

The authors declare that they have no known competing financial interests or personal relationships that could have appeared to influence the work reported in this paper.

## Acknowledgments

This study was supported by The Scientific and Technological Research Council of Türkiye (TÜBİTAK) under the 2209-A Research Project Support Programme for Undergraduate Students (Project No: 1919B012304745), and the authors would like to express their sincere gratitude for this funding.

## References

[1] Orthopedic Implants Market Size, Share & COVID-19 impact analysis, by product (joint reconstruction (knee, hip, and extremities), spinal implants (spinal fusion devices and spinal non-fusion devices), trauma implants, and others)), by end-user (hospitals. https://www.fortunebusinessinsights.com/enquiry/request-sample-book/orthopedic-implants-market-101659, 2022.
[2] N. Taherpour, Y. Mehrabi, A. Seifi, B. Eshrati, S.S. Hashemi Nazari, Epidemiologic characteristics of orthopedic surgical site infections and under-reporting estimation of registries using capture-recapture analysis, BMC Infect. Dis. 21 (2021) 1–7, https://doi.org/10.1186/s12879-020-05687-z.
[3] J.R. Lentino, Prosthetic joint infections: Bane of orthopedists, challenge for infectious disease specialists, Clin. Infect. Dis. 36 (2003) 1157–1161, https://doi.org/10.1086/374554.
[4] A. Ewald, S.K. Glückermann, R. Thull, U. Gbureck, Antimicrobial titanium/silver PVD coatings on titanium, Biomed. Eng. Online 5 (2006) 1–10, https://doi.org/10.1186/1475-925X-5-22.
[5] I. Qayoom, A.K. Teotia, A. Panjla, S. Verma, A. Kumar, Local and sustained delivery of rifampicin from a bioactive ceramic carrier treats bone infection in rat tibia, ACS Infect. Dis. 13 (2020) 2938–2949, https://doi.org/10.1021/acsinfecdis.0c00369.
[6] J.A. Dos Reis Junior, F.B. De Carvalho, R.F. Trindade, P.N. De Assis, P.F. De Almeida, A.L.B. Pinheiro, A new preclinical approach for treating chronic osteomyelitis induced by staphylococcus aureus: in vitro and in vivo study on photodynamic antimicrobial therapy (PAmT), Lasers Med. Sci. 29 (2014) 789–795, https://doi.org/10.1007/s10103-013-1422-2.
[7] B. Parsons, E. Strauss, Surgical management of chronic osteomyelitis, Am. J. Surg. 188 (2004) 57S–66S, https://doi.org/10.1016/S0002-9610(03)00292-7.
[8] T.J. Foster, M. Höök, Surface protein adhesins of Staphylococcus aureus, Trends Microbiol. 6 (1998) 484–488, https://doi.org/10.1016/S0966-842X(98)01400-0.
[9] D.P. Lew, F.A. Waldvogel, Osteomyelitis, Lancet 364 (2004) 369–379, https://doi.org/10.1016/S0140-6736(04)16727-5.
[10] L. Lazzarini, J. T Mader, J. H Calhoun, Osteomyelitis in long bones, J bone Jt, Surg Am 86 (2004) 2305–2318, https://doi.org/10.2106/00004623-200410000-00028.
[11] N.C. Lindfors, P. Hyvönen, M. Nyyssönen, M. Kirjavainen, J. Kankare, E. Gullichsen, J. Salo, Bioactive glass S53P4 as bone graft substitute in treatment of osteomyelitis, Bone 47 (2010) 212–218, https://doi.org/10.1016/j.bone.2010.05.030.
[12] B. Li, T.J. Webster, Bacteria Antibiotic Resistance: New Challenges and Opportunities for Implan.
[13] M.Q. Shah, M.S. Zardad, A. Khan, S. Ahmed, A.S. Awan, T. Mohammad, Surgical Site Infection in t-associated orthopedic infections, J. Orthop. Res. 36 (2018) 22–32, https://doi.org/10.1002/jor.23656. Orthopaedic Implants And Its Common Bacteria With Their Sensitivities To Antibiotics, In Open Reduction Internal Fixation, J. Ayub Med. Coll. Abbottabad 29 (2017) 50–53.
[14] T.F. Moriarty, R. Kuehl, T. Coenye, W.J. Metsemakers, M. Morgenstern, E. M. Schwarz, M. Riool, S.A.J. Zaat, N. Khana, S.L. Kates, G.R. Richards, Orthopaedic device-related infection: current and future interventions for improved prevention and treatment, EFORT Open Rev. 1 (2016) 89–99, https://doi.org/10.1302/2058-5241.1.000037.
[15] B. Li, T.F. Moriarty, T. Webster, M. Xing, Racing for the surface: antimicrobial and interface tissue engineering. https://doi.org/10.1007/978-3-030-34471-9, 2019.
[16] L. Drago, D. Romanò, E. De Vecchi, C. Vassena, N. Logoluso, R. Mattina, C. L. Romanò, Bioactive glass BAG-S53P4 for the adjunctive treatment of chronic

osteomyelitis of the long bones: an in vitro and prospective clinical study, BMC Infect. Dis. 13 (2013) 584, https://doi.org/10.1186/1471-2334-13-584.
[17] M. Powerski, B. Maier, J. Frank, I. Marzi, Treatment of severe osteitis after elastic intramedullary nailing of a radial bone shaft fracture by using cancellous bone graft in Masquelet technique in a 13-year-old adolescent girl, J. Pediatr. Surg. 44 (2009) E17–E19, https://doi.org/10.1016/j.jpedsurg.2009.04.039.
[18] X. He, Y. Liu, Y. Tan, L.M. Grover, J. Song, S. Duan, D. Zhao, X. Tan, Rubidium-containing mesoporous bioactive glass scaffolds support angiogenesis, osteogenesis and antibacterial activity, Mater. Sci. Eng. C 105 (2019) 110155, https://doi.org/10.1016/j.msec.2019.110155.
[19] M.S. ur Rahman, M.A. Tahir, S. Noreen, M. Yasir, M.B. Khan, T. Mahmood, A. Bahadur, M. Shoaib, Osteogenic silver oxide doped mesoporous bioactive glass for controlled release of doxorubicin against bone cancer cell line (MG-63): in vitro and in vivo cytotoxicity evaluation, Ceram. Int. 46 (2020) 10765–10770, https://doi.org/10.1016/j.ceramint.2020.01.086.
[20] M. Vallet-Regí, E. Ruiz-Hernández, Bioceramics: from bone regeneration to cancer nanomedicine, Adv. Mater. 23 (2011) 5177–5218, https://doi.org/10.1002/adma.201101586.
[21] A. Romero-Palacios, D. Petruccelli, C. Main, M. Winemaker, J. de Beer, D. Mertz, Screening for and decolonization of Staphylococcus aureus carriers before total joint replacement is associated with lower S aureus prosthetic joint infection rates, Am. J. Infect. Control 48 (2020) 534–537, https://doi.org/10.1016/j.ajic.2019.09.022.
[22] X. Wang, L. Fang, S. Wang, Y. Chen, H. Ma, H. Zhao, Z. Xie, Antibiotic treatment regimens for bone infection after debridement: a study of 902 cases, BMC Musculoskelet. Disord. 21 (2020) 215, https://doi.org/10.1186/s12891-020-03214-4.
[23] S. Steinmetz, D. Wernly, K. Moerenhout, A. Trampuz, O. Borens, Infection after fracture fixation, EFORT Open Rev. 4 (2019) 468–475, https://doi.org/10.1302/2058-5241.4.180093.
[24] R. Spitzmüller, D. Gümbel, C. Güthoff, S. Zaatreh, A. Klinder, M. Napp, R. Bader, W. Mittelmeier, A. Ekkernkamp, A. Kramer, D. Stengel, Duration of antibiotic treatment and risk of recurrence after surgical management of orthopaedic device infections: a multicenter case-control study, BMC Musculoskelet. Disord. 20 (2019) 184, https://doi.org/10.1186/s12891-019-2574-4.
[25] T.A. van Vugt, J.A.P. Geurts, J.J. Arts, N.C. Lindfors, Biomaterials in Treatment of Orthopedic Infections, Elsevier Ltd., 2017, pp. 41–68, https://doi.org/10.1016/B978-0-08-100205-6.00003-3.
[26] N. Köse, Implant-associated infections, TOTBİD Derg 10 (2011) 174–177.
[27] T. Tanı, K. Okada, S. Takahashı, N. Suzukı, Y. Shımada, E. Itoı, Doxorubicin-loaded calcium phosphate cement in the management of bone and soft tissue tumor, In Vivo 20 (2006) 55–60.
[28] S.A. Blirup- Plum, T. Bjarnsholt, H.E. Jensen, K.N. Kragh, B. Aalbæk, H. Gottlieb, M. Bue, L.K. Jensen, Pathological and microbiological impact of a gentamicin-loaded biocomposite following limited or extensive debridement in a porcine model of osteomyelitis, Bone Jt. J. 9 (2020) 394–401, https://doi.org/10.1302/2046-3758.97.BJR-2020-0007.R1.
[29] N. Jiang, X. Zhao, L. Wang, Q. Lin, Y. Hu, B. Yu, Single-stage debridement with implantation of antibiotic-loaded calcium sulphate in 34 cases of localized calcaneal osteomyelitis, Acta Orthop. 91 (2020) 353–359, https://doi.org/10.1080/17453674.2020.1745423.
[30] F. Unal, C. Tasar, B. Ercan, Fabrication and *in Vitro* characterization of antibacterial magneto-luminescent core-shell bioactive glass nanoparticles, Ceram. Int. 49 (2023) 20118–20126, https://doi.org/10.1016/j.ceramint.2023.03.135.
[31] F. Unal, B. Ercan, Magnetic and luminescence properties of bioactive glass nanoparticles for biomedical applications, J Aust Ceram Soc 61 (2025) 301–310, https://doi.org/10.1007/s41779-024-01141-4.
[32] Y.Z. Liu, Y. Li, X. Bin Yu, L.N. Liu, Z.A. Zhu, Y.P. Guo, Drug delivery property, bactericidal property and cytocompatibility of magnetic mesoporous bioactive glass, Mater. Sci. Eng. C 41 (2014) 196–205, https://doi.org/10.1016/j.msec.2014.04.037.
[33] N. Shrivastava, N.A. Shad, M.M. Sajid, A. Duong, S.K. Sharma, Design of magnetic-luminescent Nanoplatforms: Applications in Theranostics and Drug Delivery, Springer, 2020, pp. 287–309, https://doi.org/10.1007/978-3-030-39923-8_9.
[34] H. Wang, S. Zhao, J. Zhou, K. Zhu, X. Cui, W. Huang, C. Zhang, M. Rahaman, D. Wang, Biocompatibility and osteogenic capacity of borosilicate bioactive glass scaffolds loaded with Fe3O4 magnetic nanoparticles, J. Mater. Chem. B 3 (2015) 4377–4387, https://doi.org/10.1039/c5tb00062a.
[35] C. Wu, W. Fan, Y. Zhu, M. Gelinsky, J. Chang, G. Cuniberti, V. Albrecht, T. Friis, Y. Xiao, Multifunctional magnetic mesoporous bioactive glass scaffolds with a hierarchical pore structure, Acta Biomater. 7 (2011) 3563–3572, https://doi.org/10.1016/j.actbio.2011.06.028.
[36] A.C. Jayalekshmi, S.P. Victor, C.P. Sharma, Magnetic and degradable polymer/bioactive glass composite nanoparticles for biomedical applications, Colloids Surfaces B Biointerfaces 101 (2013) 196–204, https://doi.org/10.1016/j.colsurfb.2012.06.027.
[37] J. Zhang, S. Xu, K. Wang, S. Yu, Effects of the rare Earth ions on bone resorbing function of rabbit mature osteoclasts in vitro, Chinese Sci. Bull. 48 (2003) 2170–2175, https://doi.org/10.1007/BF03182845.
[38] C.A. Barta, K. Sachs-Barrable, J. Jia, K.H. Thompson, M. Wasan, C. Orvig, Lanthanide containing compounds for therapeutic care in bone resorption disorders, Dalt. Trans. (2007) 5019–5030, https://doi.org/10.1039/b705123a.
[39] S. Jebahi, H. Oudadesse, J. Elleuch, S. Tounsi, H. Keskes, P. Pellen, T. Rebai, A. El Feki, H. El Feki, The potential restorative effects of strontium-doped bioactive glass on bone microarchitecture after estrogen-deficieny induced osteoporosis: physico-Chemical and histomorphometric analyses, J. Korean Soc. Appl. Biol. Chem. 56 (2013) 533–540, https://doi.org/10.1007/s13765-013-3167-9.
[40] L.U. Khan, L.F.M. Zambon, J.L. Santos, R.V. Rodrigues, L.S. Costa, D. Muraca, K. R. Pirota, M.C.F.C. Felinto, O.L. Malta, H.F. Brito, Red-emitting magnetic nanocomposites assembled from Ag-decorated Fe3O4@SiO2 and Y2O3:Eu3+: Impact of iron-oxide/silver nanoparticles on Eu3+ emission, ChemistrySelect 3 (2018) 1157–1167, https://doi.org/10.1002/slct.201702478.
[41] R.L.S. Silva, A.T. Figueiredo, C.M. Barrado, M.H. Sousa, Luminescent and magnetic properties of Fe3O4@SiO2 phen Eu3+, Mater. Res. 20 (2017) 1317–1321, https://doi.org/10.1590/1980-5373-MR-2016-0838.
[42] A.M. Deliormanlı, B. Rahman, Fabrication and characterization of novel multifunctional superparamagnetic and fluorescent bioactive glasses for biomedical applications, J. Alloys Compd. 967 (2023) 171653, https://doi.org/10.1016/j.jallcom.2023.171653.
[43] A. Das, R. Meena, R. Kumar, B.K. Kuanr, Sensitizer-passivated magnetic ferrite/Eu 3 + -Doped oxide nanocomposite : a novel luminescent probe for facile bioimaging with superior magnetic hyperthermia performance, ACS Appl. Mater. Interfaces 17 (2025) 20872–20884, https://doi.org/10.1021/acsami.5c00587.
[44] W. Chen, H. Zhou, M. Ou, J. Zhang, C. Yang, Synthesis and characterization of magneto-optical bifunctional Fe3O4/Gd2O3:Tb3+@SiOx nanocomposites for enhanced MR imaging, Mater. Sci. Eng. B 316 (February) (2025) 118162, https://doi.org/10.1016/j.mseb.2025.118162.
[45] S.K. Swain, G. Phaomei, S.K. Dash, S.K. Tripathy, Synthesis of magnetic luminescent nanoparticle Fe3O4@LaF3:Eu,Ag@APTES@β-CD, a potential carrier of antimicrobial drug ciprofloxacin, Indian J. Microbiol. 64 (4) (2024) 1637–1645, https://doi.org/10.1007/s12088-024-01202-z.
[46] J. Molina-González, A.A. Rivera, G. Ramírez-García, A solvothermal method for the synthesis of dual paramagnetic and upconverting luminescent β-NaYF4:Yb3+,Ln3+@NaGdF4 (Ln3+=Er3+ or Tm3+) core@shell nanoparticles, Ceram. Int., vol. 50 (April) (2024) 44339–44346, https://doi.org/10.1016/j.ceramint.2024.08.282.
[47] P. Woźny, K. Soler-Carracedo, M. Perzanowski, J. Moszczyński, S. Lis, M. Runowski, Bifunctional upconverting luminescent-magnetic FeS2@NaYF4:Yb3+,Er3+ core@shell nanocomposites with tunable luminescence for temperature sensing, J. Mater. Chem. C 12 (31) (2024) 11824–11835, https://doi.org/10.1039/d4tc01117a.
[48] D.D. Yengkhom, G.S. Ningombam, R. Heisnam, N. Sharma, F.A.S. Chipem, N. R. Singh, Folic acid-conjugated magnetic-luminescent nanocomposites from Mn0.8Fe2.2O4 and GdVO4:Dy3+ with efficient heat generation and cytocompatibility in MDA-231 cell lines, Colloid Polym. Sci. 302 (2) (2024) 277–288, https://doi.org/10.1007/s00396-023-05197-9.
[49] S. Prasad S, S. Datta, T. Adarsh, P. Diwan, K. Annapurna, B. Kundu, K. Biswas, Effect of boron oxide addition on structural, thermal, in vitro bioactivity and antibacterial properties of bioactive glasses in the base S53P4 composition, J. Non-Cryst. Solids 498 (2018) 204–215, https://doi.org/10.1016/j.jnoncrysol.2018.06.027.
[50] A. Kumar, V. Gajraj, A. Das, D. Sen, H. Xu, C.R. Mariappan, Silver, copper, magnesium and zinc contained electroactive mesoporous bioactive S53P4 glass–ceramics nanoparticle for bone regeneration: bioactivity, biocompatibility and antibacterial activity, J. Inorg. Organomet. Polym. Mater. 32 (2022) 2309–2321, https://doi.org/10.1007/s10904-022-02295-z.
[51] B.K. Kizilduman, M.E. Diken, M. Dogan, M.B. Coban, Terbium (III) and salicylamide doped nickel ferrite (NiFe2O4) nanoparticles synthesized from Olea europaea L. plant extracts via eco-friendly green synthesis approach and co-precipitation method, J. Environ. Chem. Eng. 12 (2024) 113715, https://doi.org/10.1016/j.jece.2024.113715.
[52] A.M. Deliormanlı, B. Rahman, S. Oguzlar, M.Z. Ongun, Investigation of the structural, photoluminescence properties, bioactivity and 5-fluorouracil delivery behavior of $Dy^{3+}$ and Dy:$Eu^{3+}$-doped bioactive glasses, J. Alloys Compd. 944 (2023) 169153, https://doi.org/10.1016/j.jallcom.2023.169153.
[53] A. Baranowska, M. Lesniak, M. Kochanowicz, J. Zmojda, P. Miluski, D. Dorosz, Crystallization kinetics and structural properties of the 45S5 bioactive glass and glass-ceramic fiber doped with Eu3+, Materials 13 (2020) 1281, https://doi.org/10.3390/ma13061281.
[54] P. Aryal, H.J. Kim, A. Khan, S. Saha, S.J. Kang, S. Kothan, Y. Yamsuk, J. Kaewkhao, Development of Eu3+-doped phosphate glass for red luminescent solid-state optical devices, J. Lumin. 227 (2020) 117564, https://doi.org/10.1016/j.jlumin.2020.117564.
[55] Y. Wu, Z. Sun, K. Ruan, Y. Xu, H. Zhang, Enhancing photoluminescence with Li-doped $CaTiO_3$:$Eu^{3+}$ red phosphors prepared by solid state synthesis, J. Lumin. 155 (2014) 269–274, https://doi.org/10.1016/j.jlumin.2014.06.051.
[56] L. Li, Y. Pan, X. Zhou, C. Zhao, Y. Wang, S. Jiang, A. Suchocki, M.G. Brik, Luminescence enhancement in the Sr2ZnW1−xMoxO6:Eu3+,Li+phosphor for near ultraviolet based solid state lighting, J. Alloys Compd. 685 (2016) 917–926, https://doi.org/10.1016/j.jallcom.2016.06.255.
[57] Y. Xue, Y. Du, J. Yan, Z. Liu, P.X. Ma, X. Chen, B. Lei, Monodisperse photoluminescent and highly biocompatible bioactive glass nanoparticles for controlled drug delivery and cell imaging, J. Mater. Chem. B 3 (2015) 3831–3839, https://doi.org/10.1039/c5tb00204d.
[58] C.S. McCamy, Correlated color temperature as an explicit function of chromaticity coordinates, Color Res. Appl. 17 (1992) 142–144, https://doi.org/10.1002/col.5080170211.
[59] P. Dixit, V. Chauhan, S.B. Rai, P.C. Pandey, Realization of neutral white light emission in CaMoO4:4Dy3+ phosphor via Sm3+ co-doping, J. Alloys Compd. 897 (2022) 162820, https://doi.org/10.1016/j.jallcom.2021.162820.

[60] Y.F. Wu, Y.T. Nien, Y.J. Wang, I.G. Chen, Enhancement of photoluminescence and color purity of CaTiO 3: eu phosphor by li doping, J. Am. Ceram. Soc. 95 (2012) 1360–1366, https://doi.org/10.1111/j.1551-2916.2011.04967.x.

[61] M.B. Coban, M.E. Diken, S. Dogan, H. Kara Subasat, Structural, thermal, optical and antibacterial properties of Co-doped (Dy3+/Eu3+): PEG + PVA novel transparent hybrid films, J. Inorg. Organomet. Polym. Mater. 33 (2023) 2924–2942, https://doi.org/10.1007/s10904-023-02724-7.

[62] T.S. Sreena, P.P. Rao, A.K.V. Raj, T.R.A. Thara, Narrow-band red-emitting phosphor, Gd3Zn2Nb3O14:Eu3+ with high color purity for phosphor-converted white light emitting diodes, J. Alloys Compd. 751 (2018) 148–158, https://doi.org/10.1016/j.jallcom.2018.04.135.

[63] S.L. Iconaru, M. Motelica-Heino, D. Predoi, Study on europium-doped hydroxyapatite nanoparticles by fourier transform infrared spectroscopy and their antimicrobial properties, J. Spectrosc. 2013 (2013) 284285, https://doi.org/10.1155/2013/284285.

[64] J. Li, Q. Zhu, Y. Wu, F. Lin, L. Liu, L. Chen, S. Wang, L. Song, Synthesis, characterization, and applications of rare-earth-based complexes with antibacterial and antialgal properties, ACS Appl. Bio Mater. 7 (2024) 104–113, https://doi.org/10.1021/acsabm.3c00424.

[65] L.S. Arias, J.P. Pessan, A.P.M. Vieira, T.M.T. De Lima, A.C.B. Delbem, D. R. Monteiro, Iron oxide nanoparticles for biomedical applications: a perspective on synthesis, drugs, antimicrobial activity, and toxicity, Antibiotics 7 (2018) 46, https://doi.org/10.3390/antibiotics7020046.